The Astrophysical Journal, 987:7 (14pp), 2025 July 1 https://doi.org/10.3847/1538-4357/add5f3

Main-oval Auroral Emission from a T6 Brown Dwarf: Observations, Modeling, and Astrometry

J. C. Guirado[1,2], J. B. Climent[1], J. D. Bergasa[3], M. A. Pérez-Torres[4,5,6], J. M. Marcaide[7], and L. Peña-Moñino[4]
[1] Departament d'Astronomia i Astrofísica, Universitat de València, C. Dr. Moliner 50, E-46100 Burjassot, València, Spain
[2] Observatori Astronòmic, Universitat de València, Parc Científic, C. Catedrático José Beltrán 2, E-46980 Paterna, València, Spain
[3] Universidad Internacional de Valencia (VIU), C/ Pintor Sorolla 21, E-46002 Valencia, Spain
[4] Instituto de Astrofísica de Andalucía, Consejo Superior de Investigaciones Científicas (CSIC), Glorieta de la Astronomía s/n, E-18008, Granada, Spain
[5] Facultad de Ciencias, Universidad de Zaragoza, Pedro Cerbuna 12, E-50009 Zaragoza, Spain
[6] School of Sciences, European University Cyprus, Diogenes street, Engomi, 1516 Nicosia, Cyprus
[7] Real Academia de Ciencias Exactas, Físicas y Naturales de España, Calle Valverde 22, E-28004, Madrid, Spain
Received 2025 January 24; revised 2025 May 2; accepted 2025 May 6; published 2025 June 23

Abstract

From a series of 5 GHz Very Long Baseline Array (VLBA) radio observations taken over a 1 yr span, we present the detection of compact, highly polarized radio emission from the T6 brown dwarf WISE J112254.72+255022.2, compatible with electron cyclotron maser emission. Both the total and polarized lightcurves show variability in correspondence with a rotation period of 1.95 ± 0.03 hr. Comparison with models indicates that the quasi-steady radio emission of this brown dwarf is produced in circumpolar auroral rings, with remarkable similarity to the main-oval auroras in Jupiter. We have detected a large 100% polarized flare in one of the VLBA epochs (2022.82), which may imply the existence of active longitudes in the auroral rings with a nonaxisymmetric beaming cone radiation pattern, similar to the dusk/dawn asymmetries seen in the Jovian radio emissions. We also present a high-precision astrometric analysis of the sky motion of WISE J112254.72+255022.2, resulting in revised values of proper motion and parallax with an improvement in precision of 1 order of magnitude. The common kinematics of WISE J112254.72+255022.2 with its wide companion, the M dwarf LHS 302, is confirmed with submilliarcsecond precision, suggesting that this brown dwarf may have formed by gravitational fragmentation of the outer part of a protostellar disk around LHS 302. The astrometric analysis imposes very tight bounds on the presence of low-mass companions around WISE J112254.72+255022.2, ruling out objects more massive than Saturn. Our results strengthen the analogy between radio-emitting brown dwarfs and the magnetized planets of our solar system.

Unified Astronomy Thesaurus concepts: Radio astrometry (1337); Aurorae (2192); Very long baseline interferometry (1769); Radio continuum emission (1340); Brown dwarfs (185)

1. Introduction

Ultracool dwarfs (UCDs) are defined as cosmic bodies with spectral type later than M7V, encompassing very-low-mass stars, brown dwarfs, and planetary objects (J. D. Kirkpatrick et al. 1997). The M7V spectral type indicates the beginning of processes related to the decreasing effective temperature (<2700 K), in particular the appearance of dust clouds, which significantly influence the atmospheric chemistry and its evolution (e.g., C. Helling et al. 2008). UCDs with the latest spectral types can be considered as scaled-up exoplanet analogs, excellent targets to better understand a wide range of phenomena related to formation mechanisms, low gravity, dusty atmospheres, or planetary magnetism (J. A. Caballero 2018).

UCDs are fully convective objects, with no shearing layer between convective and radiative regions, able to generate a magnetic field from the dynamo processes known to occur in stars with earlier spectral types. The discovery of radio emission from a M9V dwarf (E. Berger et al. 2001) constituted a relative surprise, as the radio detection violated the empirical Güdel–Benz relationship between X-rays and radio luminosities, in turn suggesting that magnetic activity and, correspondingly, radio emission were not precluded in UCDs. Subsequent radio surveys showed that ∼10% of the observed UCDs are radio emitters (P. K. G. Williams & E. Berger 2015; M. Route & A. Wolszczan 2016a; M. M. Kao & E. L. Shkolnik 2024). This radio emission is consistent with the presence of a quiescent component, attributed to unpolarized gyrosynchrotron emission, and another pulsed, highly polarized emission produced by the electron cyclotron maser (ECM) instability (D. B. Melrose & G. A. Dulk 1982; henceforth cited as MD82). Highlighting the analogy of some UCDs with (exo) planets, the ECM mechanism is known to operate in the magnetized planets of the solar system (e.g., L. Lamy et al. 2011; M. S. Marques et al. 2017), and it is postulated to be present in exoplanets (P. Zarka 2007; J. D. Nichols 2011).

Radio emission of UCDs is frequently associated with short rotation periods (J. S. Pineda et al. 2017). However, not all rapid rotator UCDs are detectable radio emitters (M. McLean et al. 2012), emphasizing the importance of other factors at play, such as the plasma conditions and the strength and topology of the magnetic field. In principle, the association between low multipole order fields and radio emission is supported by both the dipolar magnetic fields seen in the planets of the solar system and the success in modeling the emission of radio luminous UCDs assuming a dipolar configuration (i.e., S. Turnpenney et al. 2017). However, global nonaxisymmetric magnetic topologies have been inferred (C. Lynch et al. 2015), suggesting that more complex magnetic configurations might also be present in radio-emitting UCDs.

Table 1
Journal of Observations

Antennas	Project/Segment	Observing Date	UT Range	Synthesized Beam (mas,°)
VLBA	BG278 A	08 Apr. 2022 (2022.27)	03:30–07:30	4.1 × 1.8, –0.9
VLBA[a]	BG278 B	06 Jul. 2022 (2022.51)	21:30–01:30	3.8 × 1.6, –2.6
VLBA[a]	BG278 C	25 Oct. 2022 (2022.82)	14:30–18:30	3.8 × 1.5, –3.3
VLBA[a]	BG278 D	09 Jan. 2023 (2023.02)	09:30–13:30	3.6 × 1.5, –3.0
VLBA[b]	BG278 E	15 Apr. 2023 (2023.29)	03:00–07:00	4.2 × 2.2, –7.9

Notes.
[a] VLBA-KP did not participate.
[b] VLBA-MK did not participate.

The enhanced sensitivity of interferometers operating primarily at GHz frequencies (J-VLA, ATCA), and the advent of Square Kilometre Array precursors (LOFAR, ASKAP), optimized at MHz to GHz frequencies, have boosted the detection of UCDs, showing evidence of radio emission in objects with increasingly cooler spectral types including, among others, a T2.5-type candidate to planetary mass object (M. M. Kao et al. 2018), a T5.5 + T7.0 binary (H. K. Vedantham et al. 2023), and a T8 dwarf (K. Rose et al. 2023).

In addition to the abovementioned radio interferometers, the high brightness temperature of the radio emission measured in a number of UCDs (see references below) enables the use of the very long baseline interferometry (VLBI) technique. The high spatial resolution that VLBI provides is a suitable tool to constrain both the magnetic and kinematic properties of the UCDs; actually, VLBI observations have contributed to remarkable results, namely, the establishment of direct limits on the radio emission brightness temperature (TVLM 513 −46546; J. Forbrich & E. Berger 2009), the measurement of precise dynamical mass in a binary system (2MASS J0746 +2000AB; Q. Zhang et al. 2020), the discovery of the first planetary companion from radio astrometry (TVLM 513 −46546; S. Curiel et al. 2020), and the discovery of the first extrasolar radiation belts (LSR J1835+3259; J. B. Climent et al. 2023; M. M. Kao et al. 2023).

In this context, the application of VLBI astrometry to the coolest UCDs results in special interest. T dwarfs are excellent targets for astrometric searches of exoplanets, since their low mass facilitate the presence of lower-mass planets (Saturn to Earth mass) orbiting them; additionally, the submilliarcsecond precision inherent to VLBI astrometry allows us to detect companions throughout a wide range of planetary masses, covering objects formed through different mechanisms, i.e., from giant planets (mass ratio $q \sim 0.1$), probably formed as binary systems via fragmentation of cloud cores (P. Padoan & Å. Nordlund 2004), to Saturn-mass planets ($q \sim 0.01$), probably formed as bona fide planets via a protoplanetary disk (P. M. Harvey et al. 2012).

Given the considerations above, and to increase the statistics of UCDs with compact radio emission, we initiated a VLBI program to observe nearby, fast-rotating ultracool dwarfs, covering spectral types from M7 to T6. In this paper, we focus on WISE J112254.72+255022.2 (J. D. Kirkpatrick et al. 2011; hereafter WISE J1122), a T6-type brown dwarf located at 15.9 pc (W. M. J. Best et al. 2020). The radio emission of WISE J1122 was discovered at GHz frequencies with the Arecibo telescope (M. Route & A. Wolszczan 2016b; henceforth cited as RW16), with follow-up detection with the Very Large Array (VLA; P. K. G. Williams et al. 2017; henceforth cited as WGB17). Periodic radio bursts from WISE J1122 have been observed with both instruments, although reporting different rotation periods: 17.3 minutes, from pulsar timing techniques using Arecibo, and 116 minutes, from the lightcurve measured with the VLA. In any case, the extreme rotation rate of WISE J1122 along with its late spectral type convert this object into a prime target to investigate magnetic phenomena in the realm of brown dwarfs.

We report on the detection of milliarcsecond-scale highly polarized radio emission from WISE J1122 with variability in correspondence with its rotation period. This radio emission is compatible with ECM emission produced in circumpolar auroral rings, with remarkable similarity to the main oval auroras in Jupiter. We also present a high-precision astrometric analysis of the sky motion of WISE J1122, resulting in revised values of proper motion and parallax. Bounds on the presence of lower-mass companions are discussed.

2. Observations and Data Reduction

We carried out a series of Very Long Baseline Array (VLBA) observations at the *C* band (5 GHz) during 2022 and 2023 (project code BG278; see Table 1 for details). We used a standard continuum setup for the 6 cm band, with eight subbands of width 128 MHz recorded in dual circular polarization at 2 bits per sample for a total data rate of 4 Gbps per antenna. We used the phase-reference technique, interleaving scans of WISE J1122 and the extragalactic source J112553.7+261019 (angular separation of $0.^{\circ}75$), the latter with coordinates included in the third realization of the International Celestial Reference Frame (P. Charlot et al. 2020). The duty cycle lasted 6 minutes, with 4 minutes on the target, and approximately 1 minute on the phase calibrator, providing a total integration time on WISE J1122 of ∼220 minutes per epoch.

The data were calibrated using the NRAO Astronomical Image Processing System (G. van Moorsel et al. 1996) following routines included in the `VLBARUN` pipeline: (i) we performed amplitude calibration using system temperatures and antenna gains provided by each station; (ii) we corrected the ionospheric dispersion using GPS-based Global Ionospheric Maps; (iii) we updated the Earth orientation parameters at the time of the observations; (iv) we corrected for the parallactic angle; (v) we performed a fringe search on the calibrator integrated over each scan to remove residual contributions to the phases; and (vi) we interpolated these solutions from the calibrator onto the target data.

The calibrated visibilities were subsequently imaged and deconvolved with the Common Astronomy Software

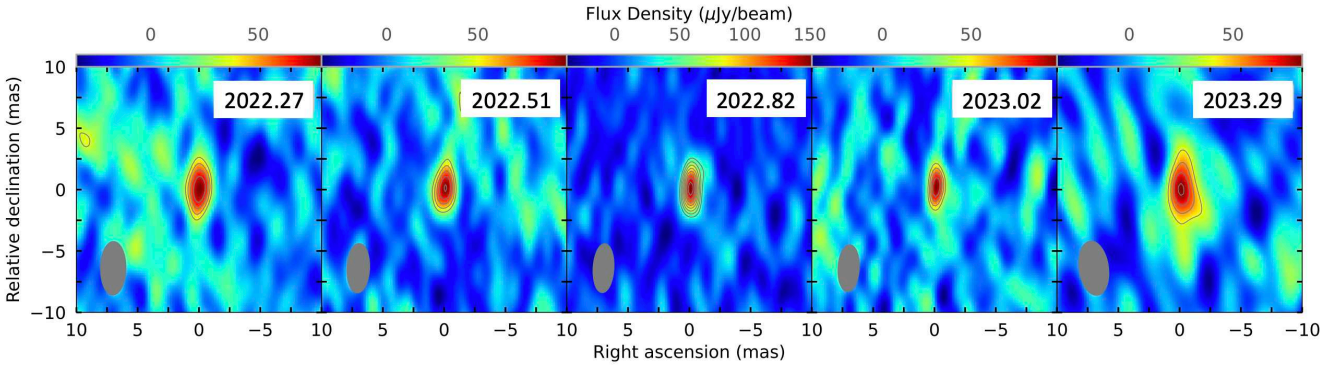

Figure 1. Reconstructed total flux (Stokes *I*) images centered on WISE J1122 coordinates corresponding to each of the VLBA observing epochs. The contours represent detection levels at 3σ, 4σ, 5σ, 6σ, etc. The gray ellipses in the lower-left corners represent the FWHM beam sizes (image properties are summarized in Table 2).

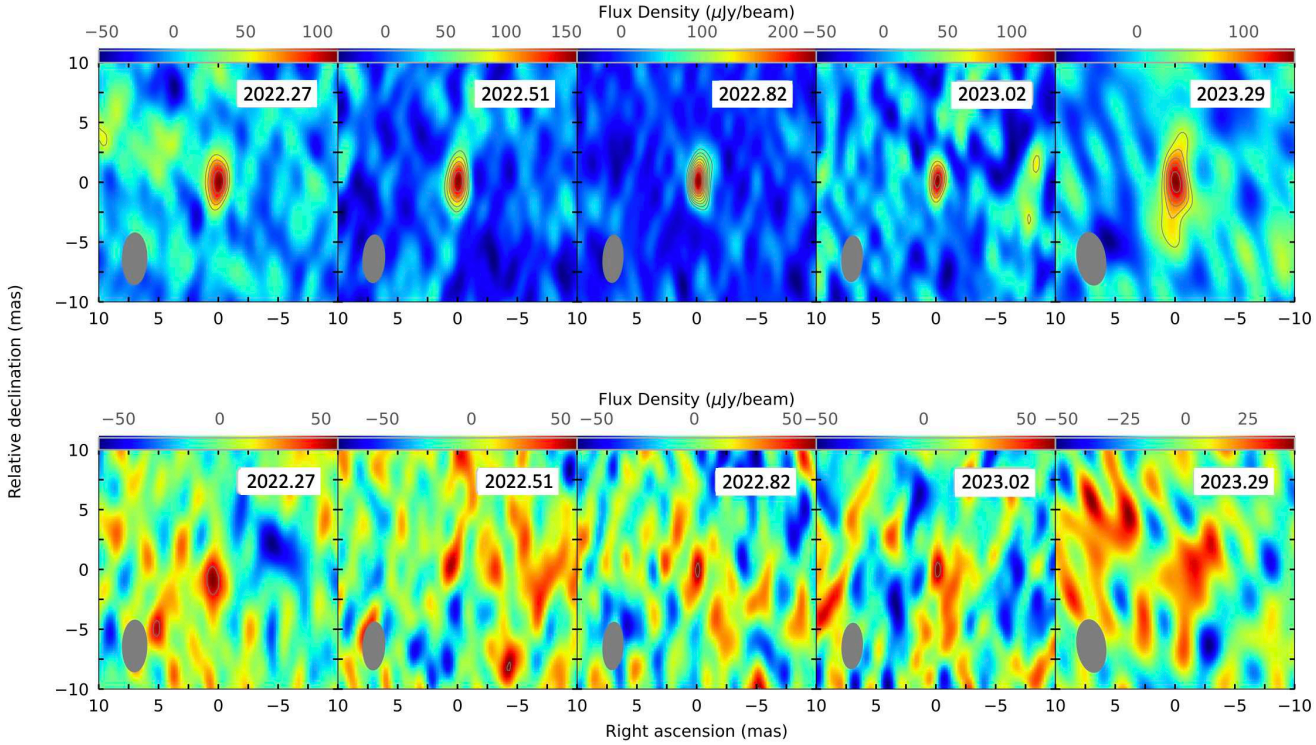

Figure 2. Reconstructed RCP (upper row) and LCP (bottom row, showing nondetections) images centered on the coordinates of WISE J1122 corresponding to each of the VLBA observing epochs. The contours represent detection levels at 3σ, 4σ, 5σ, 6σ, etc. The gray ellipses in the lower-left corners represent the FWHM beam sizes (image properties are summarized in Table 2).

Applications (CASA) package (J. P. McMullin et al. 2007). We employed naturally weighted, wide-field images to search for compact radio emission of the brown dwarf WISE J1122 by examining the area around its anticipated coordinates. The latter were obtained from the (radio) position given in WGB17, propagated to each observing epoch using the proper motion and parallax values provided by J. D. Kirkpatrick et al. (2011). In all five VLBA epochs, a single unresolved point source is detected well within the uncertainties of the expected positions of WISE J1122 (initially $\sim 0\farcs3$ precise, but substantially improved after subsequent VLBA detections); considering the large proper motion of this source (exceeding 1" yr^{-1}), the association of our VLBA detections with radio emission from WISE J1122 is corroborated. Finally, we used the `tclean` algorithm to obtain phase-referenced, channel-averaged, total flux images of WISE J1122 (see Figure 1). We again performed the procedure above to obtain images at both right and left circular polarization (RCP and LCP, respectively; see Figure 2). Image parameters are shown in Table 2. We emphasize that, during this phase-reference mapping process, the positional information of WISE J1122 with respect to the external quasar is conserved, thus relating the position of WISE J1122 to the ICRF (see Section 4.4).

3. Results

Figure 1 reveals detections in Stokes *I* of an unresolved source in all observing epochs. The flux density averaged $\sim 80\,\mu$Jy, except for segment C, which shows a significant increase in flux reaching $137 \pm 18\,\mu$Jy. These are the first VLBI images of WISE J1122, which confirm the presence of compact and persistent radio emission in such a cool T6 object. Circularly polarized maps (Figure 2) show that RCP emission

Table 2
WISE J1122 Image Parameters

Project	Stokes *I*		RCP		LCP	
	S_{peak}[a] (μJy beam^{-1})	σ[b] (μJy beam^{-1})	S_{peak}[a] (μJy beam^{-1})	σ[b] (μJy beam^{-1})	S_{peak}[a] (μJy beam^{-1})	σ[b] (μJy beam^{-1})
BG278A	79 ± 15	12	114 ± 18	12	66	15
BG278B	99 ± 12	14	157 ± 18	14	<57[c]	19
BG278C	152 ± 18	14	241 ± 25	14	62	16
BG278D	98 ± 14	14	134 ± 17	14	60	16
BG278E	93 ± 20	14	148 ± 20	14	<57[c]	19

Notes.
[a] Peak of brightness.
[b] rms noise.
[c] 3σ upper bound.

dominates in all BG278 segments, with flux densities ranging from 100 to 220 μJy, again with segment C showing the maximum values. In contrast, LCP emission is only marginally detected in segments A, C, and D with flux densities slightly above the detection threshold ($3\sigma \sim 50\,\mu$Jy beam^{-1}). This points toward highly polarized radio emission.

Indeed, previous observations already reported circularly polarized pulsed radio emission from WISE J1122. WGB17 detected 4–8 GHz time-variable radio emission from WISE J1122, showing primarily RCP bursts ($\sim$500 μJy) alongside a weaker LCP emission ($\sim$100 μJy). These authors report a periodicity of $\sim$116 minutes. On the other hand, in the course of a 5 GHz search from flaring emission in L and T dwarfs conducted with the Arecibo telescope, M. Route & A. Wolszczan (2016b) detected several 15%–100% LCP bursts from WISE J1122 with flux densities $\sim$1.5–3 mJy, and an estimated period of $\sim$17.3 minutes, a value near the rotational breakup limit, assuming WISE J1122 to be a highly oblate object older than 1 GHz (RW16). In turn, we examined the presence of radio bursts and time variability in our VLBA flux density data.

3.1. Time Variability

We used the CASA routine `uvmodelfit` to obtain time series of spectrally averaged Stokes *I* and RCP flux values of WISE J1122 at all epochs. We selected the time resolution given by each scan length ($\sim$180 s), as a balance between the signal-to-noise ratio (SNR) and sensible monitoring. Given the low SNR of the LCP data, `uvmodelfit` did not produce usable Stokes *V* and LCP time series. Instead, for the sake of a better representation of the polarization properties of WISE J1122, we recovered both time series using the well-known relationships in the quasi-monochromatic approach $I = \frac{1}{2}(\mathrm{RCP} + \mathrm{LCP})$ and $V = \frac{1}{2}(\mathrm{RCP} - \mathrm{LCP})$.

Given the previous lightcurves reported in RW16 and WGB17, the radio emission of WISE J1122 is expected to be rotationally modulated; therefore, we searched for periodicities in our flux density data to appropriately combine the five observing epochs folded to the most favorable rotation rate. We used a Lomb–Scargle approach (N. R. Lomb 1976; J. D. Scargle 1982) to find the period(s) inherent to the time evolution of the radio flux density. We present in Figure 3 the resulting periodogram for the RCP data set, that with the highest SNR, where we found two dominant peaks with a false-alarm probability (FAP) $\sim$1%: the first one corresponds to 1.95 ± 0.03 hr and the second one at 0.98 ± 0.04 hr (i.e., 117 and 59 minutes, respectively); the uncertainties were derived from the FWHM of the peaks and the average SNR of the data points (J. T. VanderPlas 2018). Our longer period of 1.95 hr is in excellent agreement with the WGB17 estimate from VLA observations, and we interpret it as the putative rotation period of WISE J1122, while the shorter period of 0.98 hr is associated with intraperiod flux variations, as discussed in Section 3.2. Our data do not favor the extremely short period of 17.3 minutes reported by RW16; these authors also proposed an alternative rotation rate of 0.863 hr, which is close, but not coincident (3σ difference), to the second peak of our periodogram (0.98 ± 0.04 hr).

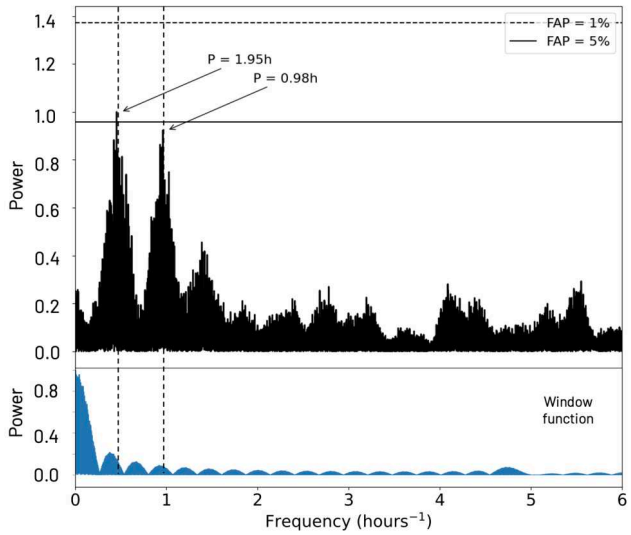

Figure 3. Generalized Lomb–Scargle periodogram of the spectrally averaged time series of RCP data sampled with a time resolution of $\sim$180 s. Time series of the five observing epochs have been combined in the periodogram. FAP of 1% and 5% are plotted for reference. We interpret the largest peak (1.95 hr) as the most probable rotation period of WISE J1122 (in coincidence with WGB17's estimate) while the second peak (0.98 hr) would show the presence of intraperiod variability. The periodogram of the window function is also shown.

3.2. Total and Polarized Lightcurves

We present our VLBA lightcurves in Figure 4, where the data of all observing epochs are phase wrapped to a rotation period of 1.95 hr. Binned median values are also shown in Figure 4; we understand that this averaging may smooth out rapid flares and/or underestimate the flux values at certain

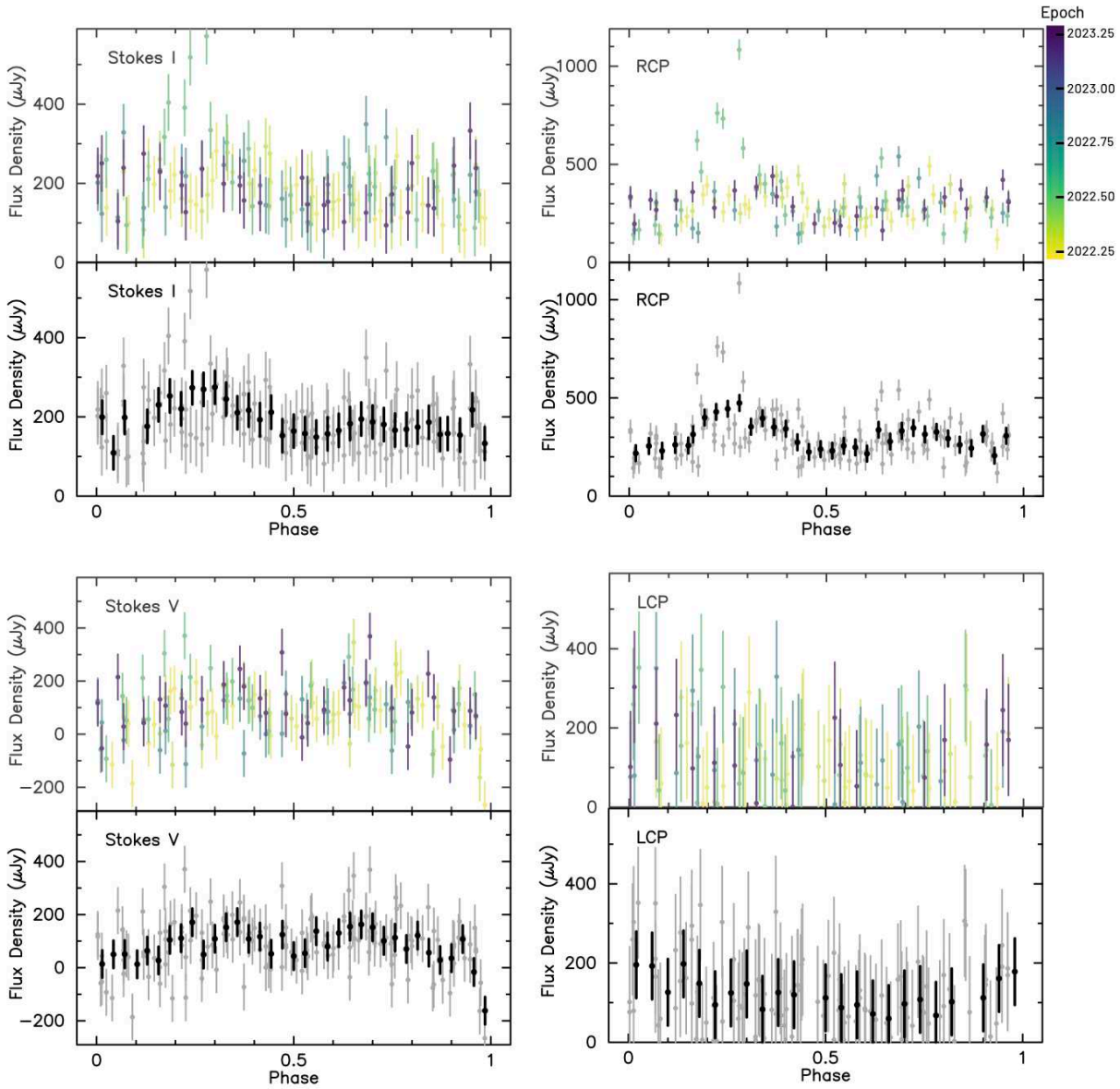

Figure 4. Periodicity of the flux density of WISE J1122. Stokes I/V and RCP/LCP lightcurves of all epochs phase wrapped to a rotation period of 1.95 hr. Stokes V and LCP lightcurves are obtained from the combination of Stokes I and RCP observed data. For each panel, the upper plots show the lightcurve of each of the five observing epochs according to the color scale; the lower plots show the averaged binned values (black) along with the individual curves (gray). An intraperiod sinusoidal trend is present in the data (reflected in the secondary peak of the periodogram in Figure 3); this sinusoid is most evident in the RCP lightcurve, peaking in rotation phases ∼0.3 and ∼0.7 with 6σ and 3σ over the rms noise, respectively.

rotation phases, but it highlights longer-term trends, providing a valuable view of the quasi-steady emission of WISE J1122 averaged over one year, the time span of our observations.

The averaged RCP lightcurve shows a sinusoidal trend that peaks in rotation phases ∼0.3 and 0.7. Since this is the predominant polarization handedness in the radio emission of WISE J1122, both peaks are also visible in Stokes I and V; actually, Stokes V is positive (i.e., preference for RCP) during 90% of the rotation period. The shorter period of 0.98 hr in our periodogram would reflect the time separation of these two maxima within the same rotation. In contrast, the reconstructed lightcurve in LCP shows almost negligible flux values for most of the period, showing a weak increase in coincidence with the depths of RCP around rotation phases 0.1 and 0.9. The presence of these sinusoidal patterns in the averaged flux densities suggests that whatever the acting radiation mechanism, it must be capable of producing polarized radio emission in most of the rotation phases, with stable intensity on average, on timescales of one year. This statement is supported by the similarity of the RCP/LCP VLBA lightcurves with those obtained with the VLA in 2016 (Figure 1 in WGB17) which also present a RCP double-peaked profile; being the similarity of both lightcurves a remarkable coincidence, we notice that both the uncertainties associated with the rotation period and the long time baseline between our data and WGB17's do not allow us to phase-align both profiles.

Having said the above, we note that the VLBI lightcurves present excursions from the average values as a consequence of the variable nature of the radio emission; the most remarkable feature is the 100% RCP burst with flux density >1 mJy seen in phase 0.3 in segment C (see Figure 5, where,

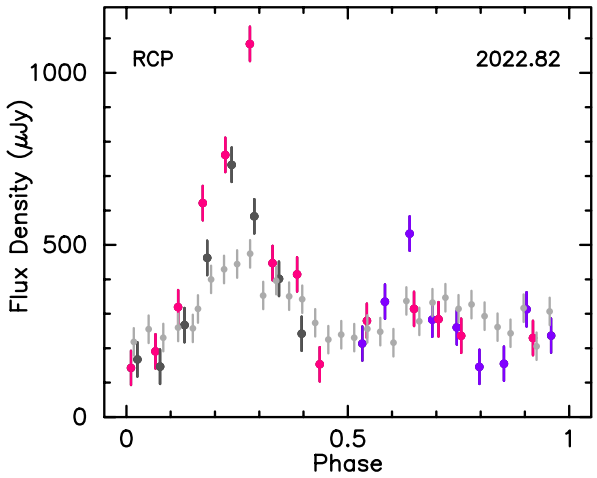

Figure 5. Detail of the RCP lightcurve corresponding to segment C (epoch 2022.82). Different colors correspond to different, but consecutive periods (chronologically, purple–red–dark gray). The averaged lightcurve is shown in light gray.

for clarity, the lightcurve for this particular epoch is plotted separately). We discuss this particular feature in Section 4.3.

4. Discussion

4.1. The Radio Emission of WISE J1122

The average flux densities stated in the previous section imply a mean radio luminosity of $\sim 10^{13.7}$ erg s^{-1} Hz^{-1} at 15.9 pc. Taking the flux density measured in the large burst in segment C, the radio luminosity rises to $\sim 10^{14.5}$ erg s^{-1} Hz^{-1}, a value that is similar to those reported in RW16 and WGB17, and comparable to other radio-emitting T dwarfs (K. Rose et al. 2023; H. K. Vedantham et al. 2023).

If the emitting region is unresolved, the resolution of an interferometer and the measured flux density provide a lower limit of the brightness temperature of the radio emission (A. Lobanov 2015). For the case of WISE J1122, based solely on these interferometric arguments, our data impose that $T_{\rm B} > 2.5 \times 10^8$ K. Further assuming that the size of the emitting region corresponds to the typical size of a T8 object ($\sim 1\,R_{\rm J}$; I. Baraffe et al. 2002), the lower bound of the brightness temperature becomes $T_{\rm B} > 8 \times 10^{10}$ K, comparable to the more stringent bound of $T_{\rm B} > 4 \times 10^{11}$ K determined by RW16 based on the intense flares detected with Arecibo.

The smoothly varying behavior of the lightcurves in Figure 4 may lead to considering gyrosynchrotron emission as a possible radiation mechanism. However, gyrosynchrotron emission, canonically associated with a quiescent, unpolarized component of the UCD radio emission, is unlikely to account for both the high $T_{\rm B}$ above and the persistent circular polarization of WISE J1122. Rather, the explanation of these properties requires a coherent mechanism that powers the radio emission. The two processes typically considered are plasma emission and ECM (MD82).

Plasma radiation originates from plasma waves excited by high-energy electron density (Langmuir) waves (S. A. Kaplan & V. N. Tsytovich 1969); plasma emission is radiated at the harmonics of the plasma frequency ν_p, defined as $\nu_p = 9000\, n^{1/2}$ Hz, with n the plasma density in cm^{-3}. The brightness temperature is above 10^{13} K for a wide range of plasma conditions; emission at the first harmonic could be 100 % circularly polarized (e.g., A. V. Stepanov et al. 2001). ECM emission is produced from a population of high-energy electrons with a loss-cone anisotropy (i.e., deficiency of electrons with small pitch angle); the maser emission is activated at the first harmonics of the gyrofrequency $\nu_g = 2.8 \times 10^6\, B$ MHz (with B the magnetic field in Gauss) provided that $\nu_g \gg \nu_p$ (MD82). The maser growth rate strongly depends on the angle of the wavevector $\hat{k}$ with the magnetic field, therefore producing highly beamed radiation that is emitted following a hollow cone pattern attached to the local magnetic field line. ECM radiation is strongly circularly polarized, reaching extremely large brightness temperatures of $T_{\rm B} \sim 10^{18}$ K (MD82). The handedness of the polarization depends on the magneto-ionic mode amplified by the ECM mechanism (either ordinary, *o*-mode, or extraordinary, *x*-mode, in turn depending on the direction of the local magnetic field). Our data do not allow us to distinguish which magneto-ionic mode is favored (different plasma conditions suppress one mode or the other). However, regardless of the mode being excited, radiation originating in opposite magnetic hemispheres will have opposite handedness.

Therefore, both coherent mechanisms justify our high $T_{\rm B}$ limits and high circular polarization properties. However, the rotational modulation seen in our averaged lightcurves (Figure 4) is naturally explained by the beamed ECM emission instead, whose direction is determined by the magnetic field lines. Effectively, the modulation is produced by the changing relative geometry between the line of sight and the magnetic field line(s) as the brown dwarf rotates. Such a directionality is difficult to justify with the nonbeamed plasma emission. Thus, although the presence of plasma radiation cannot be ruled out, our data favor the ECM mechanism as the main source of compact radio emission in WISE J1122. Assuming that ECM is radiated at the first harmonic of ν_g, and taking our largest observing frequency band (5.1 GHz), we obtain a lower bound for the magnetic field of $B > 1.8$ kG (similar to the values reported in RW16 and WGB17). Likewise, using the condition for ECM $\nu_g \gg \nu_p$, we find that the electron density in the region where the maser is generated should accomplish that $n \ll 3 \times 10^{11}$ cm^{-3}; this condition is likely to be met in WISE J1122, considering the plasma densities estimated for late-type M dwarfs ($\sim 10^{5-7}$ cm^{-3}; J. B. Climent et al. 2022) or even those of massive hot magnetic stars ($\sim 10^9$ cm^{-3}; P. Leto et al. 2020).

4.2. The Auroral Ring Model

Several authors (J. D. Nichols et al. 2012; S. Turnpenney et al. 2017) hypothesize that the quasi-steady ECM emission in UCDs, like that we detect in WISE J1122, follows a mechanism similar to that responsible for Jupiter decameter (DAM) non-Io emission (S. W. H. Cowley & E. J. Bunce 2001). Details of this model can be found in the references above; we outline them briefly here: the model assumes the existence of an equatorial plasma disk that corotates with the magnetosphere around the central object. The origin of the plasma is attributed to a companion object, with a role similar to that of Io in the Jovian system. The plasma expands radially outward by centrifugal forces as its angular velocity decreases to conserve angular momentum. The shear in rotational flow resulting from the departure of the plasma from rigid corotation induces radially directed currents in the plasma sheet (associated with $E = -v \times B$, with v the relative velocity between the plasma and the magnetosphere, and B the local

magnetic field). The presence of a gradient of the plasma angular velocity produces an azimuthal component of the magnetic field near the magnetic equator, which effectively manifests in a bending of the magnetic field lines. The currents associated with this azimuthal magnetic field consist of upward-directed currents from the equator following the magnetic field lines toward higher magnetospheric latitudes, returning from the magnetosphere to the plasma sheet to close the circuit. The high-energy electrons in these upward field-aligned currents feed auroral phenomena. A similar circuit is induced in the southern magnetic hemisphere. This approach justifies Jupiter's non-Io DAM auroras and is thought to be at work in UCDs.

Based on the physics described above, we followed the geometric model proposed in S. Bloot et al. (2024) to reproduce the total and polarized lightcurves of WISE J1122. According to the references above, the auroral emission originates in circumpolar rings (which may remind the main oval in Jupiter) around the magnetic poles, where the electrons supplied by the field-aligned currents bounce back to the equatorial plasma disk. The rings are loci of constant magnetic intensity that intersect the magnetic field lines at a certain magnetic colatitude. Every point belonging to the rings is assumed to be an emitter of ECM radiation along a conical shell whose axis is tangent to the local magnetic field line; all ECM emitters are considered equivalent in intensity and radiation pattern (i.e., same hollow cone). In a dipolar magnetic field, the radiation coming from the northern or southern auroral ovals will have different circular polarization, as B would point in opposite directions with respect to the wavevector $\hat{k}$ of the emission (B pointing outward/inward for the northern/southern magnetic hemisphere), hence producing a different handedness. The model assumes that x-mode emission dominates, meaning that, according to the International Astronomical Union (IAU) convention, the radiation from the northern/southern hemisphere is positive/negative Stokes V, i.e., RCP/LCP. The choice of the o-mode would have produced equivalent results, just with opposite handedness.

The parameters involved in this geometrically oriented model are the inclination of the rotation axis (i), the obliquity of the magnetic field axis (β), the colatitude of the auroral oval (θ_B), the half-opening angle of the ECM emission cone (α), and the thickness of the conical shell ($\Delta\alpha$). For each point on the auroral rings, ECM radio emission is observed when the angle between the line of sight and the hollow cone axis is in the range $\alpha \pm \Delta\alpha$ (that is, the radio emission of the hollow cone reaches the observer). Observed radio emission from the northern/southern ring is counted as RCP/LCP, respectively.

Taking both the Stokes I and RCP averaged lightcurves as input, we used the `magnetic-geometry-retrieval` code[8] (R. D. Kavanagh et al. 2024) to estimate the most probable values of the geometric parameters defined above (details are provided in the Appendix). The results of our analysis are shown in Table 3 and illustrated in Figure 6. The spin axis is slightly inclined toward the observer ($i = 86.^{\circ}8$), with a magnetic axis obliquity of $\beta = 2.^{\circ}6$, so that radiation from the northern magnetic hemisphere has a better chance to reach the observer, as expected by the predominance of RCP. Likewise, the weaker LCP flux densities seen in Figure 4 are a consequence of the less favorable orientation of the LCP radiation patterns originating at the southern auroral ring. Both RCP and LCP alternate during the rotation period, due to the changing orientation of the magnetic axis as the brown dwarf rotates.

[8] https://github.com/robkavanagh/magnetic-geometry-retrieval/

Table 3
Inferred Geometric Parameters of the Auroral Ring Model for WISE J1122

Parameter	Prior	Posterior
Spin axis inclination (i)	$\mathcal{U}(0, 90)$	$86.^{\circ}8 \pm 0.^{\circ}6$
Magnetic axis obliquity (β)	$\mathcal{U}(0, 60)$	$2.^{\circ}6 \pm 0.^{\circ}5$
Magnetic colatitude of the auroral ring (θ_B)	$\mathcal{U}(0, 40)$	$2.^{\circ}7 \pm 0.^{\circ}6$
Hollow cone half-opening angle (α)	$\mathcal{U}(30, 90)$	$86.^{\circ}0 \pm 0.^{\circ}7$
Hollow cone thickness ($\Delta\alpha$)	$\mathcal{U}(0, 10)$	$8.^{\circ}4 \pm 1.^{\circ}4$

Note. For each parameter, the table shows both the prior and posterior distributions resulting from the Bayesian inference. $\mathcal{U}$ denotes uniform distribution. See the Appendix.

With respect to the beaming parameters, we find a half-opening angle of $\alpha = 86.^{\circ}0$ and a cone thickness of $\Delta\alpha = 8.^{\circ}4$. In comparison, the pattern of the Jupiter ECM radio emission is observed to have a similar half-opening angle ($\alpha \sim 70°$–$90°$) with a thinner conical sheet ($\Delta\alpha \sim 1°$; B. Cecconi et al. 2012). On the other hand, R. D. Kavanagh et al. (2024) report $\alpha \sim 70°$ and $\Delta\alpha \sim 4°$ for the emission pattern of a T8 dwarf. Although our estimates are in reasonable agreement with the values above, the validity of these comparisons might be limited by the complex scenario in the maser region, with different electron velocities and/or different directions of the magnetic field.

We used the values reported in Table 3 to model the observed lightcurves (see Figure 7), whose main features at different polarizations are well reproduced. The peaks of the double lobe seen in RCP (and consequently seen in Stokes I and V) effectively correspond to the rotation phases ($\sim$0.3 and $\sim$0.7) which maximize the range of brown dwarf magnetic longitudes whose ECM emission reaches the observer. The different slopes of the RCP and Stokes V lightcurves at the extremes of the rotation phase are due to the contribution of LCP flux density. For the same reason, the Stokes I curve is flatter than the RCP curve. The overall agreement of the proposed auroral ring model and our data is remarkable.

4.3. A Closer Look at the Flare of 2022.82

The RCP lightcurve corresponding to segment C (epoch 2022.83) of our VLBA series shows a 100% polarized burst with flux density > 1 mJy that peaks in rotation phase 0.3. The duty cycle of the flare is $\sim$30% (larger than that of most UCDs; M. M. Kao et al. 2016), and it was observed during two consecutive rotations at the same phase with decreasing intensity (from $\sim$1100 to 700 μJy after one turn; see Figure 5).

The flare seen in WISE J1122 resembles similar phenomena seen in the Jupiter non-Io DAM emission, which also vary in timescales of hours. Indeed, non-Io auroras in Jupiter show a modulation in intensity that is attributed to the expansion or compression of the magnetosphere induced by the solar wind (S. W. H. Cowley & E. J. Bunce 2003). In addition, periodic bursts have been observed at determined rotation phases (M. Panchenko & H. O. Rucker 2011), suggesting the existence of active Jovian magnetic longitudes, likely corresponding to areas of the plasma sheet in subcorotation with the magnetosphere, with a more efficient generation of ECM emission. The flare seen in WISE J1122 seems to fit this latter periodic type of event, considering that the flare occurs at

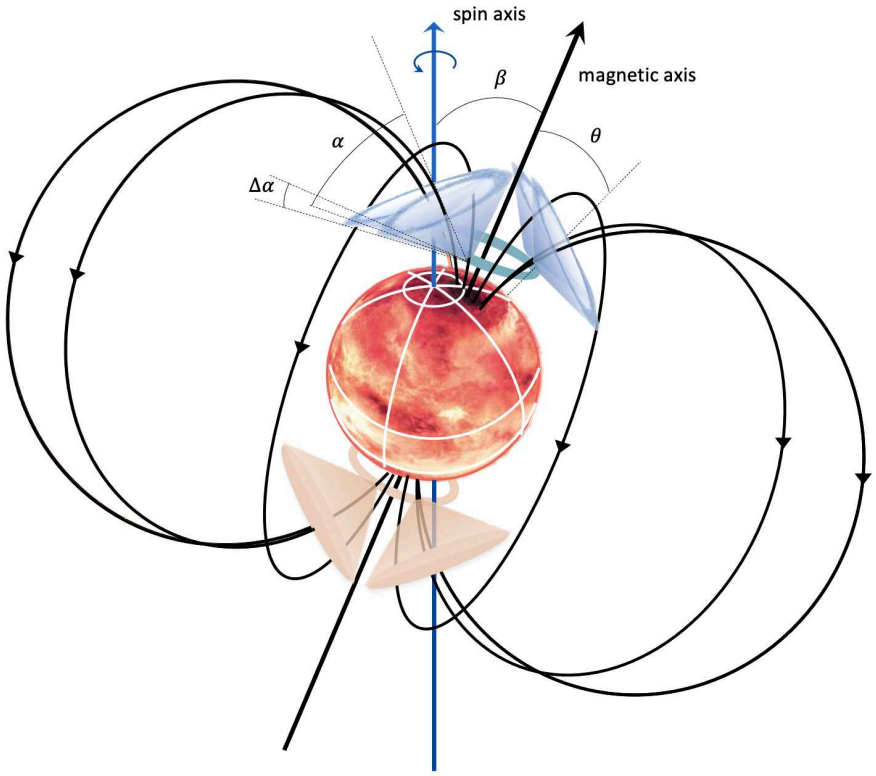

Figure 6. Representation of the auroral ring model for WISE J1122. The auroral rings are shown in both hemispheres; different colors indicate different handedness of the circular polarization (bluish/orange for RCP/LCP at the northern/southern magnetic hemisphere). Each point in the ring is an ECM emitter, although, for clarity, only a few hollow cone patterns are plotted. The values of magnetic axis obliquity, magnetic colatitude, and the geometry of the hollow cone correspond to the best-fit model of Table 3. Notice that the spin axis is inclined toward the observer. The figure is intended for illustration purposes only, and it is not to scale. Image credit: Metazoa Studio/Hugo Salais (brown dwarf surface). Used with permission.

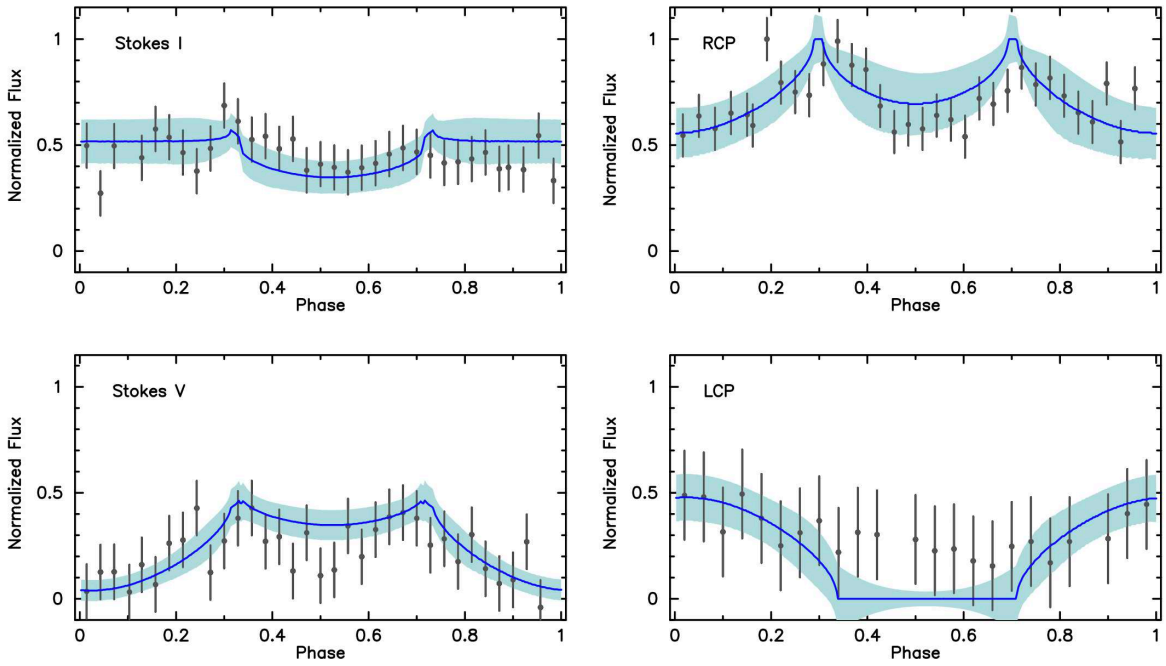

Figure 7. Normalized quasi-steady emission of WISE J1122. The data points corresponding to the flare in segment C have been removed. For each panel, the lightcurve corresponding to the best fit resulting from our analysis is plotted in blue (see Table 3). The shaded area shows 1σ variance of the model.

a particular rotation phase, which points toward a preferred range of longitudes producing enhanced ECM emission. A potential drawback of this interpretation is that we would expect to observe the flare twice per rotation (corresponding to the dawn and dusk of the ECM hollow cone emission pattern attached to the active longitudes), while only one event is observed in our lightcurve. Again, taking the non-Io emission as a guide, we find that some periodic non-Io bursts in Jupiter behave similarly, with only one peak appearing per rotation (M. Panchenko et al. 2013), being the second one absent or strongly weakened. This dawn/dusk side asymmetry of the burst suggests the presence of anisotropies in the hollow cone pattern of the enhanced ECM emission. Such anisotropies could be expected given the nonlinear dependence of the maser growth on a large number of parameters (plasma density, frequency, velocity distribution, etc); therefore, small changes of some of the parameters above may produce a substantial variation in the maser intensity and/or directivity.

Following this line of reasoning, we used the geometric model shown in the previous section to simulate the effect of an anisotropic pattern able to explain the pulse(s) profile in Figure 5 (i.e., absence of a second pulse in the same rotation). For simplicity, we simulated an increase in the intensity of the ECM emission in a range of magnetic longitudes; these active longitudes emit enhanced emission only in a particular direction (chosen to be visible by the observer), in practice generating an anisotropic hollow cone pattern (see Figure 8 for details). The dusk/dawn asymmetry introduced by this basic anisotropy suffices to suppress (or weaken) one of the two pulses, reproducing the RCP lightcurve seen in 2022.82 (see Figure 9). Other, more elaborate anisotropies, whose application to WISE J1122 is beyond the scope of this paper, have been considered in the case of Io-related ECM emission. P. H. M. Galopeau & M. Y. Boudjada (2011) proposed that Io-related ECM bursty emission could be radiated in a flattened hollow cone, i.e., a hollow cone with elliptical section whose minor axis is aligned with the local magnetic field. Similarly, a tangent plane beaming model has been proposed for the terrestrial Auroral Kilometric Radiation (R. L. Mutel et al. 2008) and the magnetic chemically peculiar star CU Vir (C. Trigilio et al. 2011). These patterns restrict the burst emission to a particular active rotation phase, resulting in a single peak per rotation in the lightcurve.

We notice that the burst seen in WISE J1122 reaches flux density values (∼mJy) similar to those reported by RW16, although some differences appear when comparing both events. First, the handedness of the flares reported in RW16 is LCP, opposite to that in segment C; second, the duration of the RW16 flares is 30–120 s, very impulsive flares in comparison with the gradual behavior of the VLBA flare, with a duration ∼700 s; and third, the detection rate in our VLBA campaign is substantially lower, while RW16 reported 5 flares in 29 observing hours, we only detected two pulses (considering two consecutive rotations in segment C) in 20 observing hours (although we may have missed other events, given our 6 minutes long observing duty cycle). WGB17 did not report any mJy bursts, indicating that the occurrence of these bursts is very occasional. The differences stated above suggest that the VLBA RCP event reported in this paper and the Arecibo LCP flares in RW16 may respond to the action of different mechanisms releasing magnetic energy into the

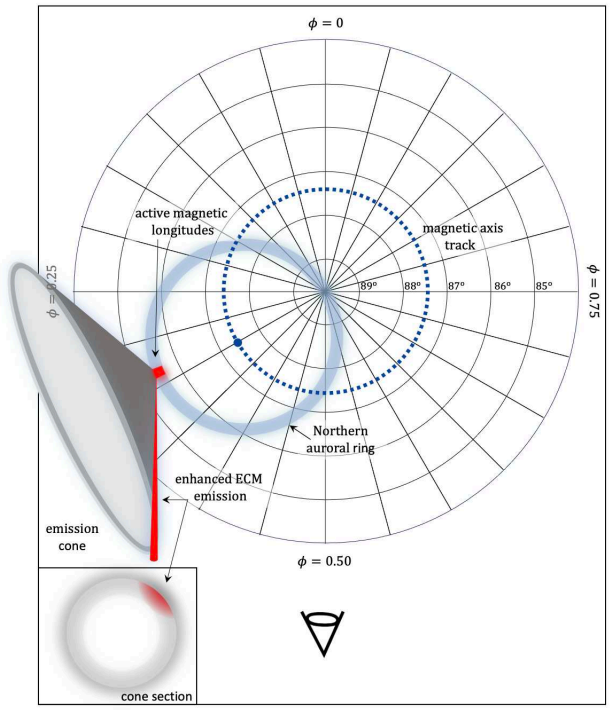

Figure 8. Polar projection of the northern aurora in WISE J1122. The grid represents the brown dwarf longitude and latitude (spin axis at latitude 90°). The track of the magnetic axis (blue dot) around the spin axis is plotted in a dark-blue dashed line; the light-blue ring corresponds to the oblique projection of the northern auroral ring. The active magnetic longitudes are marked in red color on the auroral ring; the enhanced ECM emission originating at these active longitudes (reddish color on the hollow cone) is visible by the observer, generating the large flare seen in segment C of our VLBA series (epoch 2022.82). The configuration corresponds to a rotation phase of ∼0.3; as the brown dwarf rotates, the enhanced emission is not pointing to the observer anymore, which in turn suppresses a second flare within the same rotation. Inset: section of the hollow cone showing the hot spot postulated to reproduce the lightcurve seen in epoch 2022.82.

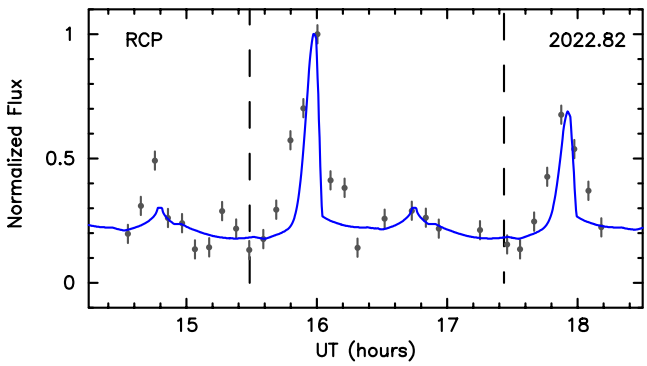

Figure 9. Following the construction shown in Figure 8, we qualitatively reproduce the lightcurve of segment C (blue continuous line). The model consists of a quasi-steady, nonflaring, auroral component (according to our best-fit parameters shown in Table 3) plus a flaring radiation originating in a certain range of active longitudes (10° in size) of the northern auroral ring. The largest flare at ∼16:00 UT is replicated assuming these active longitudes radiate following an anisotropic hollow cone pattern. The anisotropy consists of an enhancement (× 50 with respect to the average emission) of a portion of the conical sheet (10° in size; see Figure 8). The decrease of the flare intensity in the third period (∼18:00 UT) is reproduced by reducing the range of active longitudes to 5°. Multiple solutions are possible using a different range of active longitudes, burst intensities, or burst sizes. This plot shows that a simple anisotropy may generate only one flare per rotation.

Table 4
WISE J1122 J2000.0 Coordinates

Instrument	Program (epoch)	R.A. (h m s)	Decl. (° ′ ″)
VLA[a]	16A-463 (2016.36)	11 22 54.260 ± 0.015	25 50 20.0 ± 0.2
VLBA	BG278 A (2022.27)	11 22 53.819532 ± 0.000007	25 50 18.09600 ± 0.00013
VLBA	BG278 B (2022.51)	11 22 53.799128 ± 0.000007	25 50 17.99740 ± 0.00013
VLBA	BG278 C (2022.82)	11 22 53.783155 ± 0.000007	25 50 17.85634 ± 0.00013
VLBA	BG278 D (2023.02)	11 22 53.768489 ± 0.000007	25 50 17.81338 ± 0.00015
VLBA	BG278 E (2023.29)	11 22 53.742875 ± 0.000007	25 50 17.76898 ± 0.00015

Note.
[a] P. K. G. Williams et al. (2017).

Table 5
Astrometric Parameters of WISE J1122 and Its Wide Companion LHS 302

	WISE J1122[a]	LHS 302[b]
μ_α (mas yr^{-1})	−1015.62 ± 0.14	−1010.9189 ± 0.0734
μ_δ (mas yr^{-1})	−322.08 ± 0.20	−323.1270 ± 0.0684
Parallax (mas)	61.68 ± 0.10	61.6520 ± 0.0644

Notes.
[a] This paper.
[b] Gaia DR3 archive.

atmosphere of WISE J1122. However, a larger number of flares in this source would be needed to clarify their nature.

4.4. Astrometric Analysis

As we explained in Section 2, the phase-reference mapping process conserved the positional information of WISE J1122 with respect to the external quasar J112553.7+261019. Therefore, the brightness peak of the phase-referenced maps of WISE J1122 provides precise absolute coordinates referred to the ICRF. To optimize the astrometric precision, we used the RCP phase-referenced maps, the data set with the highest SNR (the use of the Stokes *I* maps provides compatible, but less precise positions). We performed an error analysis to determine the uncertainties of the radio coordinates due to errors inherent in the propagation media, the reference source structure, and the geometry of the interferometric array. We also considered the uncertainty associated with the location of the ECM emission originating in the auroral rings, in turn located at a determined height above the object surface. This height is determined by the gyrofrequency of the electrons; for M dwarfs (S. Bloot et al. 2024), heights for the fundamental frequency or its second harmonic may reach 1.2 stellar radii above the object surface. Assuming a similar scaling for WISE J1122 (height of 1.2 R_J), this translates to an uncertainty of 0.07 mas at the distance of the brown dwarf. All combined, these systematic contributions were 5 times larger than the limiting thermal noise uncertainty associated with the peak of brightness of the VLBI maps (see, e.g., R. Azulay et al. 2015). We determine a final astrometric error budget of ∼0.15 mas in each coordinate. The resulting positions of WISE J1122 and their corresponding standard deviations are shown in Table 4.

The VLBA coordinates of WISE J1122 were used to derive the proper motion, parallax via a weighted least-squares fit. We augmented our data set, including the VLA position given in WGB17, despite its relatively large uncertainty, to better constrain the large proper motion of this object. The derived astrometric parameters are shown in Table 5, and the residual postfit positions after removing the proper motion and parallax effects are shown in Figure 10. Our estimates agree within uncertainties with those provided by W. M. J. Best et al. (2020), providing an improvement in precision of 1 order of magnitude.

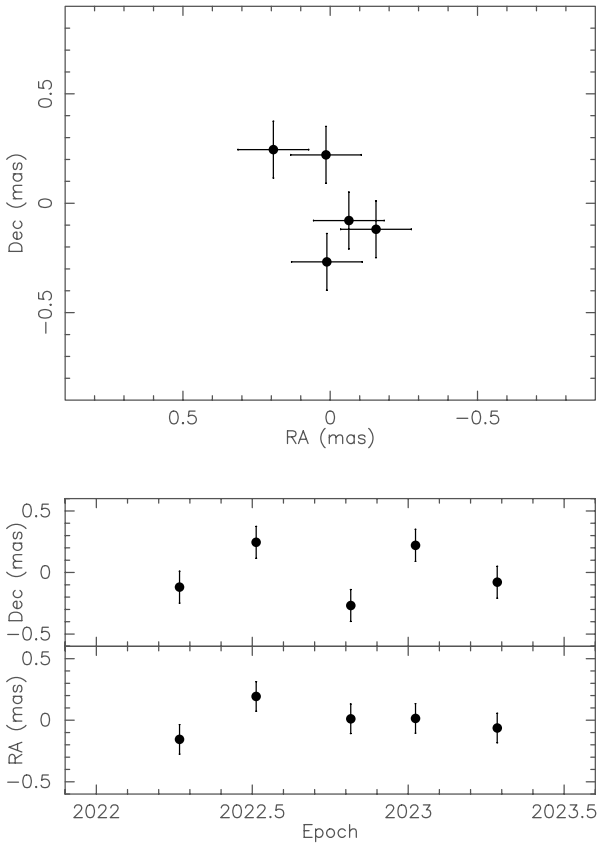

Figure 10. Astrometric residuals WISE J1122 in R.A. and decl. after subtracting proper motion and parallax effects, shown as sky motion (upper panel) and time dependence (lower panel).

4.4.1. The Wide Companion LHS 302

WISE J1122 and the M5 dwarf LHS 302 exhibit similar proper motion and parallax values; they constitute a wide pair with a projected separation of ∼4500 au (265″; J. D. Kirkpatrick

et al. 2011). The proper motion and parallax of both objects have been subsequently improved (W. M. J. Best et al. 2020), validating their similar kinematics. Our astrometric analysis of WISE J1122, along with the Gaia Data Release (DR3) astrometric parameters available for LHS 302, enables a further, submilliarcsecond-precise comparison of the kinematics of both objects. The values shown in Table 5 confirm a common distance (within uncertainties) and a very similar proper motion, with differences smaller than 0.5%. This coincidence supports the hypothesis that WISE J1122 and LHS 302 belong to the same moving group (loose associations of coeval, comoving stars; B. Zuckerman & I. Song 2004). In addition, the similar kinematics of this comoving pair of M dwarf and brown dwarf may provide clues to the formation mechanism. S. P. Goodwin & A. Whitworth (2007) propose that brown dwarfs may form as distant companions to M dwarfs by disk fragmentation; however, at large separations (>100 au), both objects are not strongly bounded and the brown dwarf may be easily disrupted by close encounters with passing stars, finally producing a comoving wide, low-mass binary system, just as LHS 302 and WISE J1122. The remarkable kinematical coincidence of both objects seems to support this hypothesis. We notice that, in this gentle disruption scenario (following S. P. Goodwin & A. Whitworth 2007), WISE J1122 may retain a circumstellar disk; therefore, the presence of companions to the brown dwarf is not excluded. We discuss this in turn.

4.4.2. Bounds to the Presence of Companions to WISE J1122

Proper motion and parallax suffice to a great extent to account for the trajectory of WISE J1122 on the sky. However, the rms of the postfit residuals in Figure 10 is 0.3 mas, comparable but larger than the uncertainties of the coordinates ($\sim 2\sigma$), thus indicating possible sub-milliarcsecond departures from the linear motion, which might be the consequence of a gravitational reflex motion. While an orbital fitting requires a larger data set, the dispersion of our astrometric residuals imposes immediate bounds to the presence of low-mass companions around WISE J1122 through Kepler's Third Law expressed as $a_* = \pi\, m_c (P^2/(m_* + m_c))^{2/3}$, with a_* the amplitude of the reflex motion of WISE J1122, π the parallax, P the period of the orbit (yr), and m_* and m_c the masses of WISE J1122 and the companion ($M_\odot$), respectively.

Assuming face-on, circular orbits, companions with mass m_c and orbital period P producing a reflex motion with amplitude a_* larger than the scatter of our astrometric residuals (0.3 mas) would be excluded; this population corresponds to the shaded area of Figure 11. Our data seem to discard companions with large values of the mass ratio q ($q > 0.1$; unless periods of a few days are considered). As an example, giant planets similar to those of the solar system are excluded, but the presence of hot Jupiters and Earth-like planets is largely allowed according to Figure 11 (in particular, a rocky planet that might constitute a potential source of plasma in the scenario discussed in Section 4.2). Saturn-like planets, similar to those discovered around TVLM 513−46546 (S. Curiel et al. 2020), would straddle the border of the exclusion area. As WISE J1122 shows as an excellent astrometric target, future observing campaigns will surely refine the constraints provided in this paper.

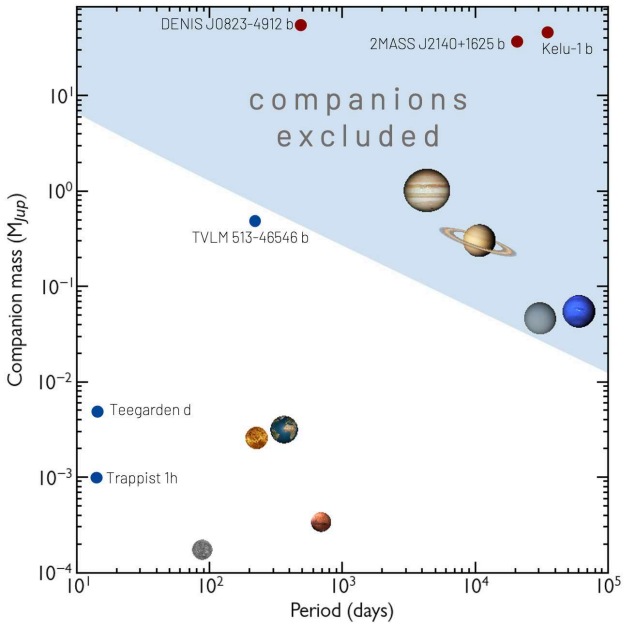

Figure 11. Companions excluded by our astrometric analysis. The shaded area shows the space of companion masses and periods producing a reflex motion larger than the rms of the astrometric residuals (~0.3 mas). Red dots indicate a selection of known binary brown dwarfs; blue dots indicate a selection of brown dwarfs with known exoplanets; solar system planets are shown for reference. Our astrometric fit discards WISE J1122 to be a binary brown dwarf, but it is largely compatible with the presence of an exoplanet with Earth-to-Saturn mass.

5. Conclusions

A series of 5 GHz VLBA phase-referenced observations of the T6 brown dwarf WISE J1122 shows that this very cool object is a persistent radio emitter, detected at all observing epochs, with radio emission originating in a very compact region, bright enough to be detected with VLBI. Our main findings can be summarized as follows:

1. The milliarcsecond-scale maps of WISE J1122 consist of a single unresolved component with circularly polarized radio emission. This radio emission is predominantly RCP, although traces of compact LCP emission are detected in some epochs.
2. We examined the time series of the RCP data set for variability and found a preferred periodicity of 1.95 ± 0.03 hr, which we assume corresponds to the rotation period of WISE J1122. The main feature of the combined, averaged lightcurves, phase wrapped to the rotation period, is a double-peak feature in RCP; the handedness of the polarization seems to alternate throughout the rotation period, with a weak increase of the LCP flux density in coincidence with the depths in the RCP lightcurve. We interpret these lightcurves as the quasi-steady auroral radio emission of WISE J1122.
3. The combined total and polarized lightcurves of WISE J1122 can be reproduced with a geometric model that assumes that the ECM emission is produced in circumpolar auroral rings, similar to the main oval auroras in Jupiter. The model fits the lightcurves remarkably well, providing estimates of the spin axis inclination, the tilt of the magnetic axis, and the

geometry of the ECM radiation pattern. If present, other radiation mechanisms apart from ECM have a residual role.

4. A large 100% RCP flare is detected in our VLBA epoch 2022.82. The flare is seen only once per rotation, which, according to the geometric parameters derived by us, may imply the existence of anisotropies in the ECM radiation pattern.
5. Our VLBA phase-referencing analysis provides submilliarcsecond-precise revised values of proper motion and parallax of WISE J1122. We have confirmed the common kinematics of WISE J1122 and the M dwarf LHS 302. According to theories of brown dwarf formation, this comoving pair of objects may have formed together, being the brown dwarf gently disrupted by gravitational interaction with passing stars.
6. The astrometric residuals in R.A. and decl. impose a limit of 0.3 mas for the reflex motion of WISE J1122 due to a possible, unseen low-mass companion. Unless very short periods are considered, this limit effectively excludes companions larger than Saturn around WISE J1122.

The results obtained for WISE J1122 emphasize the similarity between the magnetic phenomena occurring in substellar objects and those occurring in the planets of our solar system, Jupiter in particular. Indeed, very recently, radiation belts have been detected around the ultracool dwarf LSR J1835+3259 (J. B. Climent et al. 2023; M. M. Kao et al. 2023), a scaled-up version of the Jovian belts. In this paper, we demonstrate the presence of persistent main oval auroras in WISE J1122, which may respond to a very similar mechanism to those known in Jupiter. Both results support the analogy between radio-emitting brown dwarfs and the Jupiter system. Such an analogy would be complete with a confirmed detection of magnetic star-planet interaction similar to the Jovian Io auroras.

Acknowledgments

The authors thank the anonymous referee for the thorough, and constructive review of this manuscript, which improved the overall quality of the article. This work is based on observations with the Very Long Baseline Array (VLBA), which is operated by the National Radio Astronomy Observatory (NRAO). The NRAO is a facility of the National Science Foundation operated under cooperative agreement by Associated Universities, Inc. Scientific results from data presented in this publication are derived from the VLBA project code BG278. This work has made use of data from the European Space Agency (ESA) mission Gaia, processed by the Gaia Data Processing and Analysis Consortium (DPAC). Funding for the DPAC has been provided by national institutions, in particular the institutions participating in the Gaia Multilateral Agreement. J.C.G., J.B.M., and J.M.M. were supported by projects PID2020-117404GB-C22 and PID2023-147883NB-C22, funded by MCIN/AEI, CIPROM/2022/64, funded by the Generalitat Valenciana, and by the Astrophysics and High Energy Physics program by MCIN, with funding from European Union NextGenerationEU (PRTR-C17.I1) and the Generalitat Valenciana through grant ASFAE/2022/018. M.P.T. and L.P.M. were supported by projects PID2020-117404GB-C21, PID2023-147883NB-C21, and CEX2021-001131-S funded by MCIN/AEI and by the European Union (NextGenerationEU grant PRTR-C17.I1). This research made use of Astropy, a community-developed core Python package for astronomy (Astropy Collaboration et al. 2018).

Appendix
Estimate of the Geometric Parameters of the Auroral Ring Model

In Section 4.2, we used the `magnetic-geometry-retrieval` code[9] (R. D. Kavanagh et al. 2024) to derive the most probable parameters corresponding to the orientation of WISE J1122 and the geometry of the ECM hollow cone pattern. This code uses Ultranest,[10] a Monte Carlo–based algorithm which efficiently samples a wide range of the parameter space and provides posterior distributions for each model parameter via Bayesian inference. The code assumes a dipolar magnetic field corotating with the brown dwarf, where the radio emission originates in a number of active field lines. This feature was not used in the case of WISE J1122, as we consider the auroral rings to be uniform radio emitters, in the line described in S. Bloot et al. (2024). We also simplified the code to work with a single frequency band. The averaged Stokes I and RCP data were jointly used as input. We uniformly sampled the following range of the parametric space: $0^\circ \leqslant i \leqslant 90^\circ$; $0^\circ \leqslant \beta \leqslant 60^\circ$; $30^\circ \leqslant \alpha \leqslant 90^\circ$; $0 \leqslant \Delta\alpha \leqslant 10^\circ$; and $0 \leqslant \theta_B \leqslant 40^\circ$. The prior in $\Delta\alpha$ was imposed to find solutions with relatively small cone thickness (given the values reported for Jupiter and other T dwarfs; see Section 4.2). With the constraints above, we found convergence in 75 steps. The best-fit parameter estimates are shown in Table 3, which provides a reduced χ^2 of 1.31. The corresponding posterior distributions are shown in Figure 12. As a result of the prior imposed for $\Delta\alpha$, we notice that the posterior distribution of some of the fitted parameters is asymmetric. This may reflect the limited sensitivity of our averaged data to small cone thicknesses. Despite this limitation, the comparison between observed and modeled lightcurves is satisfactory (see Figure 7).

[9] https://github.com/robkavanagh/magnetic-geometry-retrieval/
[10] https://johannesbuchner.github.io/UltraNest/

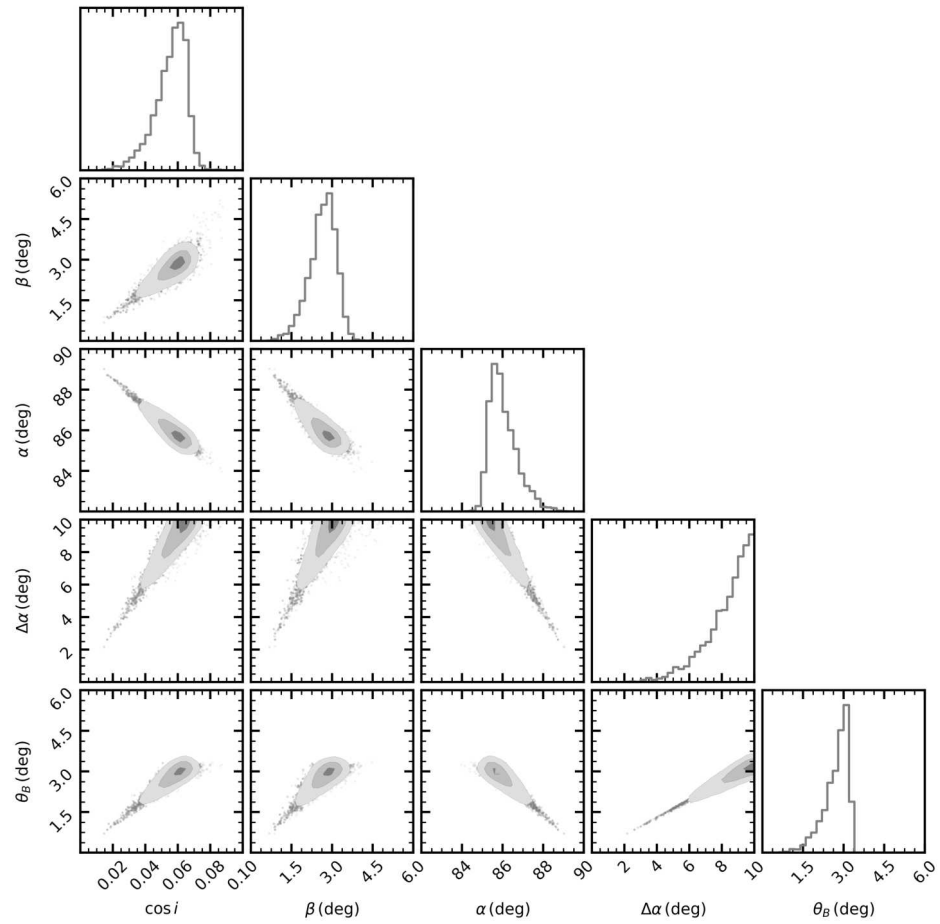

Figure 12. Corner plot showing the results of our parameter estimation for the auroral ring model. The histograms on the diagonal show the posterior distribution for each parameter. Off-diagonal plots are two-dimensional projections of the sample showing covariances; darker shading denotes regions of higher probability densities.

ORCID iDs

J. C. Guirado https://orcid.org/0000-0003-2722-1615
J. B. Climent https://orcid.org/0000-0002-5093-6208
J. D. Bergasa https://orcid.org/0009-0006-2594-3939
M. A. Pérez-Torres https://orcid.org/0000-0001-5654-0266
J. M. Marcaide https://orcid.org/0000-0002-2736-9794
L. Peña-Moñino https://orcid.org/0000-0001-6735-1655

References

Astropy Collaboration, Price-Whelan, A. M., Sipőcz, B. M., et al. 2018, AJ, 156, 123
Azulay, R., Guirado, J. C., Marcaide, J. M., et al. 2015, A&A, 578, A16
Baraffe, I., Chabrier, G., Allard, F., & Hauschildt, P. H. 2002, A&A, 382, 563
Berger, E., Ball, S., Becker, K. M., et al. 2001, Natur, 410, 338
Best, W. M. J., Liu, M. C., Magnier, E. A., & Dupuy, T. J. 2020, AJ, 159, 257
Bloot, S., Callingham, J. R., Vedantham, H. K., et al. 2024, A&A, 682, A170
Caballero, J. A. 2018, Geosc, 8, 362
Cecconi, B., Hess, S., Hérique, A., et al. 2012, P&SS, 61, 32
Charlot, P., Jacobs, C. S., Gordon, D., et al. 2020, A&A, 644, A159
Climent, J. B., Guirado, J. C., Pérez-Torres, M., Marcaide, J. M., & Peña-Moñino, L. 2023, Sci, 381, 1120
Climent, J. B., Guirado, J. C., Zapatero Osorio, M. R., et al. 2022, A&A, 660, A65
Cowley, S. W. H., & Bunce, E. J. 2001, P&SS, 49, 1067
Cowley, S. W. H., & Bunce, E. J. 2003, P&SS, 51, 57
Curiel, S., Ortiz-León, G. N., Mioduszewski, A. J., & Torres, R. M. 2020, AJ, 160, 97
Forbrich, J., & Berger, E. 2009, ApJL, 706, L205
Galopeau, P. H. M., & Boudjada, M. Y. 2011, in Planetary Radio Emissions VII, Proc. of the 7th Int. Workshop on Planetary, Solar and Heliospheric Radio Emissions (Vienna: Austrian Academy of Sciences Press), 197
Goodwin, S. P., & Whitworth, A. 2007, A&A, 466, 943
Harvey, P. M., Henning, T., Liu, Y., et al. 2012, ApJ, 755, 67
Helling, C., Ackerman, A., Allard, F., et al. 2008, MNRAS, 391, 1854
Kao, M. M., Hallinan, G., Pineda, J. S., et al. 2016, ApJ, 818, 24
Kao, M. M., Hallinan, G., Pineda, J. S., Stevenson, D., & Burgasser, A. 2018, ApJS, 237, 25
Kao, M. M., Mioduszewski, A. J., Villadsen, J., & Shkolnik, E. L. 2023, Natur, 619, 272
Kao, M. M., & Shkolnik, E. L. 2024, MNRAS, 527, 6835
Kaplan, S. A., & Tsytovich, V. N. 1969, SvPhU, 12, 42
Kavanagh, R. D., Vedantham, H. K., Rose, K., & Bloot, S. 2024, A&A, 692, A66
Kirkpatrick, J. D., Henry, T. J., & Irwin, M. J. 1997, AJ, 113, 1421
Kirkpatrick, J. D., Cushing, M. C., Gelino, C. R., et al. 2011, ApJS, 197, 19
Lamy, L., Cecconi, B., Zarka, P., et al. 2011, JGRA, 116, A04212
Leto, P., Trigilio, C., Buemi, C. S., et al. 2020, MNRAS, 499, L72
Lobanov, A. 2015, A&A, 574, A84
Lomb, N. R. 1976, Ap&SS, 39, 447
Lynch, C., Mutel, R. L., & Güdel, M. 2015, ApJ, 802, 106
Marques, M. S., Zarka, P., Echer, E., et al. 2017, A&A, 604, A17
McLean, M., Berger, E., & Reiners, A. 2012, ApJ, 746, 23
McMullin, J. P., Waters, B., Schiebel, D., Young, W., & Golap, K. 2007, in ASP Conf. Ser. 376, Astronomical Data Analysis Software and Systems XVI, ed. R. A. Shaw, F. Hill, & D. J. Bell (San Francisco, CA: ASP), 127
Melrose, D. B., & Dulk, G. A. 1982, ApJ, 259, 844
Mutel, R. L., Christopher, I. W., & Pickett, J. S. 2008, GeoRL, 35, L07104
Nichols, J. D. 2011, MNRAS, 414, 2125
Nichols, J. D., Burleigh, M. R., Casewell, S. L., et al. 2012, ApJ, 760, 59
Padoan, P., & Nordlund, Å. 2004, ApJ, 617, 559

Panchenko, M., & Rucker, H. O. 2011, in Planetary Radio Emissions VII, Proc. of the 7th Int. Workshop on Planetary, Solar and Heliospheric Radio Emissions, ed. H. O. Rucker (Vienna: Austrian Academy of Sciences Press), 157
Panchenko, M., Rucker, H. O., & Farrell, W. M. 2013, P&SS, 77, 3
Pineda, J. S., Hallinan, G., & Kao, M. M. 2017, ApJ, 846, 75
Rose, K., Pritchard, J., Murphy, T., et al. 2023, ApJL, 951, L43
Route, M., & Wolszczan, A. 2016a, ApJ, 830, 85
Route, M., & Wolszczan, A. 2016b, ApJL, 821, L21, RW16
Scargle, J. D. 1982, ApJ, 263, 835
Stepanov, A. V., Kliem, B., Zaitsev, V. V., et al. 2001, A&A, 374, 1072
Trigilio, C., Leto, P., Umana, G., Buemi, C. S., & Leone, F. 2011, ApJL, 739, L10
Turnpenney, S., Nichols, J. D., Wynn, G. A., & Casewell, S. L. 2017, MNRAS, 470, 4274
van Moorsel, G., Kemball, A., & Greisen, E. 1996, in ASP Conf. Ser. 101, Astronomical Data Analysis Software and Systems V, ed. G. H. Jacoby & J. Barnes (San Francisco, CA: ASP), 37
VanderPlas, J. T. 2018, ApJS, 236, 16
Vedantham, H. K., Dupuy, T. J., Evans, E. L., et al. 2023, A&A, 675, L6
Williams, P. K. G., & Berger, E. 2015, ApJ, 808, 189
Williams, P. K. G., Gizis, J. E., & Berger, E. 2017, ApJ, 834, 117
Zarka, P. 2007, P&SS, 55, 598
Zhang, Q., Hallinan, G., Brisken, W., Bourke, S., & Golden, A. 2020, ApJ, 897, 11
Zuckerman, B., & Song, I. 2004, ARA&A, 42, 685